Journal of Materials Chemistry A

Accepted Manuscript

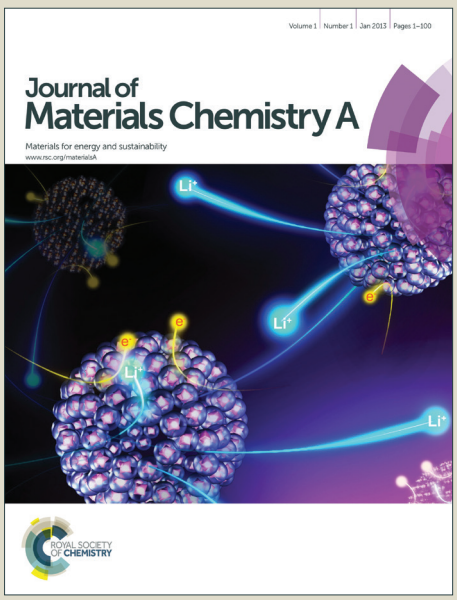

ROYAL SOCIETY OF CHEMISTRY

www.rsc.org/materialsA

Journal of

Materials Chemistry A

RSCPublishing

paper

Core-shell MnO_2@Fe_2O_3 nanospindles as positive electrode for aqueous supercapacitors

Cite this: DOI: 10.1039/x0xx00000x

Lei Zhu, [a,b,c,#] Zheng Chang, [b,#] Yanfang Wang, [b] Bingwei Chen, [b] Yusong Zhu*[a], Weiping Tang*[c] and Yuping Wu*[a,b]

Received 00th January 2015,
Accepted 00th January 2015

DOI: 10.1039/x0xx00000x

www.rsc.org/

Abstract: Supercapacitors display high power density and long cycling life that are particularly amenable to use in the field of energy storage. However, the cost is a big issue for practical application. Here, a cheap Fe_2O_3 spindle of rich natural resource is used as the positive electrode. After twined by MnO_2 nanoflakes *via* a simple and cost-effective hydrothermal method, a unique structure of core-shell MnO_2@Fe_2O_3 nanospindle has been prepared. The electrochemical performance of the nanospindle including capacitance and cycling life is markedly improved compared with the pristine Fe_2O_3 spindle. Its specific capacitance is up to 159 F g^{-1} at a current density of 0.1 A g^{-1} and especially, capacitance retention is 97.4% after 5000 cycles in a 0.5 mol L^{-1} K_2SO_4 neutral aqueous electrolyte. Combined with activated carbon as the negative electrode, the energy density can be up to 43.8 Wh kg^{-1} on the basis of weights of the two electrodes. These results reveal that the core-shell MnO_2@Fe_2O_3 nanospindle is a promising positive electrode for practical supercapacitors.

Introduction:

In the recent, the increasing consumption of conventional fossil fuel and the deteriorating environment drive people to look for new alternative energy resource. In this situation, supercapacitors come into being as a new type of electrochemical energy storage device between secondary batteries and general double layer capacitors. Nowadays, they have attracted tremendous attention by its virtue of high power density and long cycling life.[1-4]

The performance of supercapacitors strongly depends on the characteristics of the electrode materials and the electrolytes. The electrolytes used for supercapacitors can be divided into organic electrolytes and aqueous ones. The energy density of supercapacitors can be improved by increasing the working voltage and specific capacitance. The working voltage of the organic electrolytes is about 3 V while that of aqueous one is 1.23 V, but it can be expanded to 2 V by increasing the overpotentials of H_2 and O_2 evolution. As for the specific capacitance, the capacitor-type electrode materials always show higher capacitances in aqueous electrolytes due to their higher ionic conductivity. [5-7] Moreover, by the advantages of cost, safety and environmentally friendliness, aqueous solutions seem to be more suitable as electrolytes for supercapacitors. Also of note is that, since the corrosive effects of strong acidic and alkaline aqueous electrolytes like H_2SO_4 and KOH are destructive to most components of a supercapacitor,[8-10] the capacitors based on them still suffer from high-price, precipitation of materials on the electrode, electrolyte consumption, poor electrode stability, low energy density, and poor cycling life, so neutral aqueous solutions are explored as attractive electrolytes.[11-15] Given that the demand for high capacitance and high charge/discharge rate, transition metal oxides like RuO_2,[16,17] TiO_2,[18] SnO_2,[19] V_2O_5,[20] Co_3O_4,[21-24] MoO_3[25] and NiO[26,27] are considered as the ideal electrode materials for supercapacitors.[28] However, their commercial application are limited due to their high cost and environmental unfriendliness.[29-31] Hence, we must seek for cheap alternatives with higher capacitance and the possibility to be produced at a large scale, meeting the market demand.

Fe_2O_3 can be considered as a promising candidate of positive electrode for supercapacitors owing to its abundance, low cost, and environmental friendliness. However, the experimentally observed capacitance of Fe_2O_3 is considerably lower than the expected value. Its reaction kinetics is sluggish because of its low conductivity, and its cycling performance is very poor due to the possible dissolution of Fe during the charge and discharge processes. As reported, active

[a] *College of Energy, Nanjing Tech University, Nanjing 211816, Jiangsu Province, China. E-mail:* wuyp@njtech.edu.cn, *or wuyp@fudan.edu.cn*
[b] *New Energy and Materials Laboratory (NEML), Department of Chemistry & Shanghai Key Laboratory of Molecular Catalysis and Innovative Materials, Fudan University, Shanghai 200433, China.*
[c] *Shanghai Institute of Space Power-Sources (SISP), Shanghai Academy of Spaceflight Technology, Shanghai 200233, PR China. Email: wptang1962@gmail.com; Tel: +86-21-24187672*

materials with large surface area which can increase the active sites for getting electrons or for Faradaic reactions have been applied to improve the performance for supercapacitors. Recently, more and more researchers have focused on the Fe_2O_3 electrodes for supercapacitors. For example, Fe_2O_3 with different morphologies, such as nanosheets, microrods and nanorods were prepared by a simple solution-based precipitation method, and the nanosheet-based electrode delivers a specific capacitance of 116.25 F g^{-1} with cycling life up to 1000 cycles [32]. Porous iron oxide shows a capacitance up to 210 F g^{-1} in alkaline solution though the cycling performance is poor [33]. On the other hand, MnO_2 has been introduced to the positive electrode to stabilize Fe_2O_3. The research on Fe_2O_3 positive electrode with the Au film as the substrate to enhance the electrical conductivity for supercapacitors application has been reported.[34] Compared with the pristine Fe_2O_3, the composite they designed has revealed significant improvements in electrochemical properties. However, the problems of cost causing by expensive metallic film and environmental unfriendliness causing by strongly alkaline aqueous electrolytes have not been solved.

Here, using a facile hydrothermal method, a unique core-shell structured nanocomposite shaped as nanospindle was fabricated by twining MnO_2 nanoflakes around Fe_2O_3 spindles without any metallic substrates. Moreover, in 0.5 mol L^{-1} K_2SO_4 neutral aqueous electrolyte, which has been reported superior to other neutral aqueous electrolytes like Na_2SO_4 and Li_2SO_4 in terms of the fast charge-discharge process[7], the nanospindle positive electrode shows an optimized capacitance of 159 F g^{-1} much higher than that of the pristine Fe_2O_3 (55.1 F g^{-1}). In addition, compared with the former reports on Fe_2O_3 for supercapacitors, our designed MnO_2@Fe_2O_3 nanospindles, to our best knowledge, is the first report with the capacitance retention of 97.4% after 5000 cycles in a 0.5 mol L^{-1} K_2SO_4 neutral aqueous electrolyte. In addition, its energy density based on the two electrodes can be up to 43.8 Wh kg^{-1}.

Experimental

Fabrication of Fe_2O_3 spindles

Uniform Fe_2O_3 spindles were prepared by the hydrothermal method.[35] 1.46 g $FeCl_3$ was dissolved in 30 mL deionized water, then 2.16 g urea and 4.5 mL ethanediol as the protective agent were added to the Fe (Ⅲ) solution under vigorous magnetic stirring. After 30 min of magnetically stirring, the obtained suspension was transferred to a 40 mL Teflon-lined autoclave and maintained at 180 °C for 12 h. After natural cooling to room temperature, the products were collected by vacuum filtration and washed by deionized water and ethanol for several times, and then dried at 60 °C overnight.

Surface decoration of MnO_2 nanoflakes

MnO_2 nanoflakes were decorated on Fe_2O_3 spindles by a facile one-step hydrothermal method. A certain amount of Fe_2O_3 spindles as prepared were dispersed in a 0.05 mol L^{-1} $KMnO_4$ solution (30 mL). After sonication and agitation for 1 h separately, the mixture was transferred to a 40 mL Teflon-lined autoclave and maintained at 160 °C for 24 h. After abstersion and desiccation, the resulting products of MnO_2@Fe_2O_3 core-shell nanospindles were obtained. A series of composites with different MnO_2 content have been prepared by varying the amount of Fe_2O_3 added.

Materials characterization

Crystal structures of the sample X-ray diffraction (XRD) patterns were measured by a Rigaku D/MAX-IIA X-ray diffractometer with Cu-K_α radiation. Scanning electron micrographs (SEM) and transmission electron micrographs (TEM) were used to characterize the morphology of the core-shell MnO_2@Fe_2O_3 nanocomposite. The micrographs were obtained on a Philips XL30 scanning electron microscope and a JEOL JEM-2010 transmission electron microscope, respectively.

Electrochemical test

The MnO_2@Fe_2O_3 nanospindle was mixed with acetylene black and poly (tetrafluoroethylene) (PTFE) in a weight ratio of 8:1:1 in an ethanol solution. The suspension was pressed into a film after dried at 80 °C, and then it can be used as the working electrode. The substrate used for working electrode is nickel foil, and in all tests, the quality of the active material loading on the substrate is 10 mg , the area of cathode electrode is 2 cm^2, corresponding to 5 mg cm^{-2}. In the meanwhile, another nickel foil was used as the counter electrode and a saturated calomel electrode (SCE) as the reference electrode. The electrochemical tests were carried out in a three-electrode system with 0.5 mol L^{-1} K_2SO_4 solution as the electrolyte. Cyclic voltammetry (CV) was investigated at various scan rates of 1, 2, 5, 10, 20, 50, and 100 mV s^{-1} by a CHI 660D electrochemical station. LAND battery test system was employed to test galvanostatic charge-discharge and the cycling performance at various current densities of 0.1, 0.2, 0.5, 1, 1.5, 2, 2.5 and 3 A g^{-1}. A potential window in the range from 0 to 1 V was used in all the measurements. The electrochemical impedance spectroscopy (EIS) was conducted under the frequency from 10^5 Hz to 0.1 Hz, the amplitude is 5mV. The Ragone plot (power density vs. energy density) was carried out in a two-electrode full cell with the active carbon (AC) as the negative electrode and the MnO_2@Fe_2O_3 as the positive electrode, where the AC electrode was prepared by the same process as the MnO_2@Fe_2O_3 electrode.

Results and discussion

The synthesis and characterization of the pristine Fe_2O_3 spindles and the MnO_2@Fe_2O_3 nanospindle are shown in Fig. 1. All the X-ray diffraction peaks of the pristine Fe_2O_3 (Fig. 1b) can be indexed to the planes of hematite α-Fe_2O_3 (JCPDS 33-0664) without any impurities.[36] In the case of the MnO_2@Fe_2O_3 nanospindle, its diffraction peaks at 12.5 °, 25 ° and 37.6 ° corresponding to its (001), (002), (100) planes, respectively, are in agreement with δ-MnO_2,[37] suggesting the existence of Fe_2O_3 as well as MnO_2. However, these three weak diffraction peaks also indicates that the crystallinity of MnO_2 is not very high.

From the scanning electron micrographs (SEM) of the pristine Fe_2O_3 spindles (Fig. 1c), it can be seen that the pristine Fe_2O_3 exists in the form of spindles with about 800 nm in length and 400 nm in width. This morphology is similar to spherical particles and is

favorable to get high stacking density and high volumetric energy density for practical supercapacitors compared with the nanorods and nanosheets.[32] After the further hydrothermal process, MnO_2 nanoflakes were twinned around every spindle-like Fe_2O_3 particle uniformly with hardly any detached nanoflakes, and a stable protective shell was formed (Fig. 1d). This unique and ordered core-shell structured nanospindle provides an abundant porous surface area for the contact between the electrode and electrolyte, which is

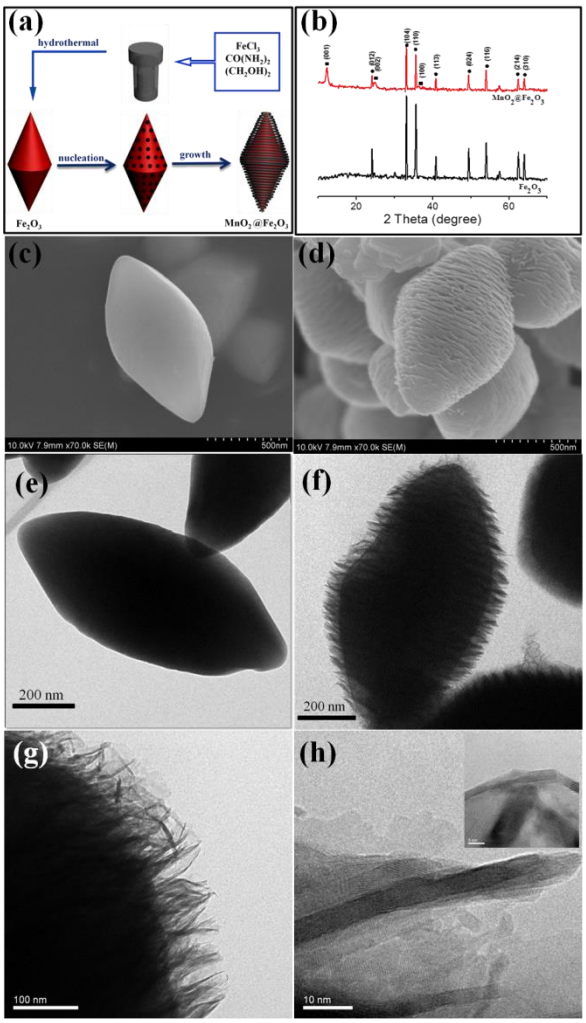

Fig. 1 Synthesis and characterization of the pristine Fe_2O_3 spindles and the MnO_2@Fe_2O_3 nanospindle: (a) Schematic illustration of the prepared process of the MnO_2@Fe_2O_3 nanospindle, (b) XRD patterns of the pristine Fe_2O_3 spindles and the MnO_2@Fe_2O_3 nanospindles, SEM micrographs of (c) the pristine Fe_2O_3 spindles and (d) the MnO_2@Fe_2O_3 nanospindles, TEM micrographs of (e) the pristine Fe_2O_3 spindles and (f) the MnO_2@Fe_2O_3 nanospindles, and HRTEM micrographs of the MnO_2@Fe_2O_3 nanocompupa (g, h).

of great significance in accelerating the electrochemical reaction. Transmission electron micrographs (TEM) further confirm the configuration of the core-shell structure of the MnO_2@Fe_2O_3 nanospindle. Fig. 1e demonstrates that the surface of the pristine Fe_2O_3 spindle particle is very smooth and Fig. 1f and 1g indicates that MnO_2 nanoflakes rolled into nanotubes automatically. They are twined around Fe_2O_3 spindles homogeneously, indicating the formation of good quality MnO_2@Fe_2O_3 core-shell nanospindle, which is well consistent with the SEM micrographs. High-resolution TEM (HRTEM) micrographs (Fig. 1h) show that the nanotubes prepared by MnO_2 nanoflakes are usually 2-3 nm wide. From the micrograph inset, we can see that the lattice fringes are not very clear and successive, indicating the poor crystalline nature of the prepared MnO_2 nanoflakes, which is basically consistent with the XRD results.

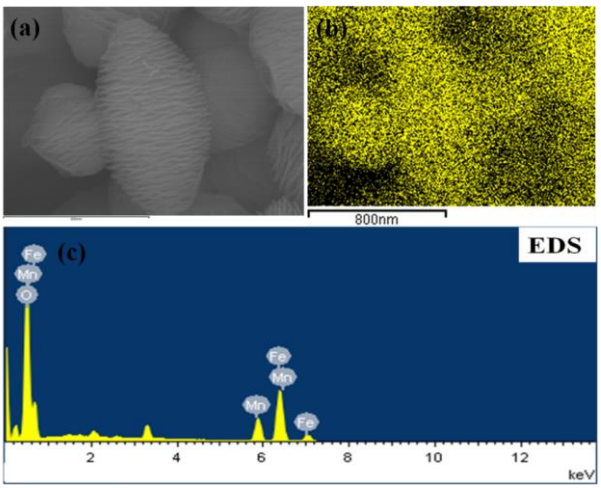

Fig. 2 (a) The SEM micrograph of the 40 wt.% MnO_2@Fe_2O_3 nanospindles, (b) the EDS mapping of Mn, and (c) the EDS spectrum of the MnO_2@Fe_2O_3 nanospindle.

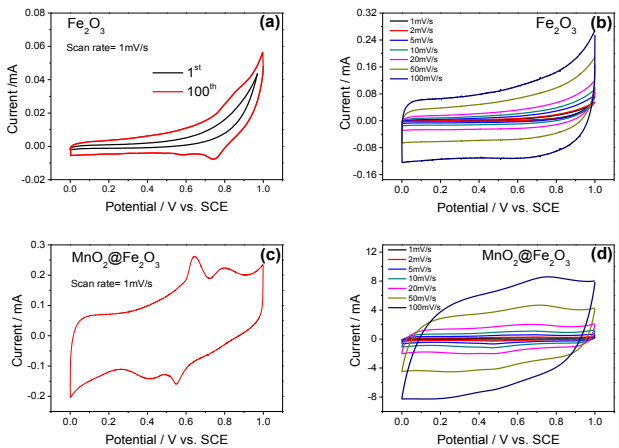

Fig. 3 Cyclic voltammetric (CV) curves of (a, b) the prepared pristine Fe_2O_3 spindles, and (c, d) the MnO_2@Fe_2O_3 nanospindles in 0.5 mol L^{-1} K_2SO_4 solution with a nickel foil as the counter electrode and a saturated calomel electrode (SCE) as the reference electrode.

From the energy dispersive spectrometer (EDS) mapping of the 40 wt.% MnO_2@Fe_2O_3 nanospindles (Fig. 2), it can be seen that the yellow dots assigned to the Mn element, is uniformly distributed on the surface of the MnO_2@Fe_2O_3 nanospindles. EDS spectrum (Fig. 2c) also displays the presence of Fe and Mn elements in the core-shell nanospindle, and the MnO_2 coating content in the nanospindle is about 40 wt.%, which is nearly consistent with the added amount.

Fig. 3 shows the CV curves of the pristine Fe_2O_3 and the MnO_2@Fe_2O_3 nanospindle. In the case of the pristine Fe_2O_3, its CV curves do not show the normal regular shape and the area is quite small and the redox peaks of different valence states of iron [Fe(II)↔Fe(III)] does not appear until after 100 cycles, suggesting its slow redox kinetics. After decorated by MnO_2 nanoflakes, two distinct pairs of Faradaic redox peaks emerge even in the first cycle at the scan rate of 1 mV s^{-1} (Fig. 3c). The possible redox reactions can be described as follows:

$$Fe_2O_3 + M^+ + e^- \longleftrightarrow Fe_2O_3M \quad M^+ = K^+ \text{or } H_3O^+ \qquad (1)$$

$$MnO_2 + M^+ + e^- \longleftrightarrow MnOOM \quad M^+ = K^+ \text{or } H_3O^+ \qquad (2)$$

The dramatic change between the two samples is evidently resulted from the surrounding MnO_2 nanoflakes on the Fe_2O_3 spindles, causing the fast reaction kinetics and significant improvement of the specific capacitance. With the increase of the scan rate, the CV curves of the pristine Fe_2O_3 spindles and the MnO_2@Fe_2O_3 nanospindles increase correspondingly, indicating the good capacitive behavior of the two electrodes. As for the MnO_2@Fe_2O_3 positive electrode, the oxidation and reduction peaks become blurred as the scan rate increases to 100 mV s^{-1} and the anodic and cathodic peaks move to higher and lower potentials, respectively, leading to a larger potential separation between redox peaks. Moreover, the profiles exhibit nearly symmetrical rectangular shapes, mostly attributing to the typical electrical double-layer capacitive behavior, which depends on the adsorption of the ions happened on the surface of the electrodes.[38] This is because the MnO_2@Fe_2O_3 nanospindle with unique structure can deliver a larger surface area to facilitate the adsorption of ions, resulting in better electrochemical performance.

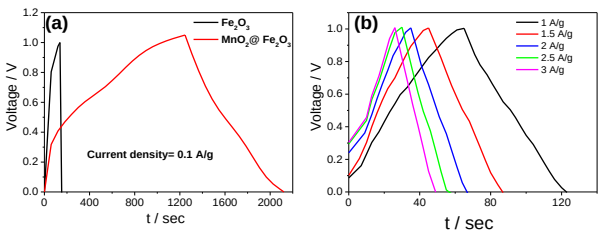

Fig. 4 (a) Comparison between the charge/discharge curves of the prepared pristine Fe_2O_3 spindles and the MnO_2@Fe_2O_3 nanospindles at the current density of 0.1 A g^{-1}, and (b) constant current charge/discharge curves of the prepared MnO_2@Fe_2O_3 nanospindles at different current densities.

The comparison of the charge/discharge curves of the nanospindle and the pristine Fe_2O_3 electrode is shown in Fig. 4a. At the low current density of 0.1 A g^{-1}, the charge/discharge time is greatly prolonged compared to that of the pristine Fe_2O_3, proving the higher capacitance. Besides, from the charge/discharge curves of the MnO_2@Fe_2O_3 electrode, it can be discerned that there are two, corresponding to the conversion between Fe(II)↔Fe(III) and Mn(IV)↔Mn(III), respectively, in accordance with the CV curves. The constant-current charge/discharge curves of the prepared MnO_2@Fe_2O_3 nanospindles at different current densities (Fig. 4b) show much better symmetry compared with the pristine Fe_2O_3, owing to the improved reversible redox reactions.

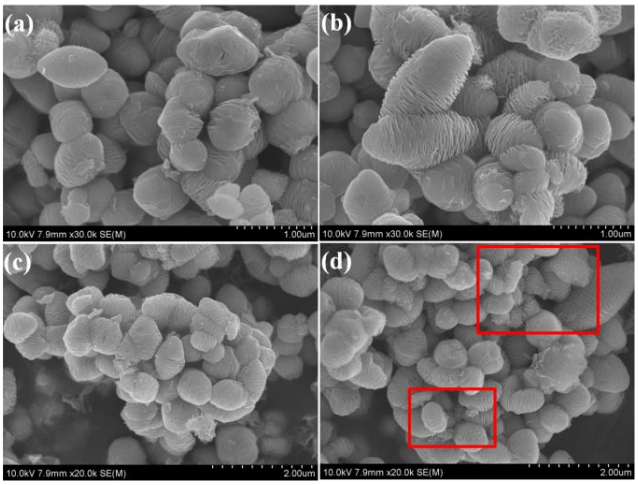

Fig. 5 SEM micrographs of the MnO_2@Fe_2O_3 nanocomposites with different MnO_2 content: (a) 10 wt.%, (b) 20 wt.%, (c) 40 wt.%, and (d) 60 wt.%.

To obtain the suitable ratio of Fe_2O_3 to MnO_2, a series of nanocomposites with different MnO_2 content have been prepared, and their morphologies examined by SEM are presented in Fig. 5. When the MnO_2 content is 10 wt.% (Fig. 5a), the MnO_2 nanoflakes were coated on the surface of the Fe_2O_3 spindles, forming a thin film-like coating shell. With the increase of the MnO_2 content, the coating film becomes rough, and a part of the MnO_2 nanoflakes rolled into nanotubes automatically, twining round the Fe_2O_3 spindles. When the content is up to 40 wt.%, the above phenomenon become more common and obvious and an appropriate and well-distributed configuration with core-shell structure comes into being (Fig. 5c). However, as the MnO_2 content is further increased to 60 wt.% (Fig. 5d), except Fe_2O_3 spindles twined by the MnO_2 nanoflakes, there are some other shapes marked with red boxes. The reason is presumably that some MnO_2 nanoflakes merged together to form MnO_2 nanoclusters. Therefore, it can be concluded that 40 wt.% MnO_2 is the optimal choice to get homogeneous morphology and the possible growth mechanism diagram is shown in Fig. 6.

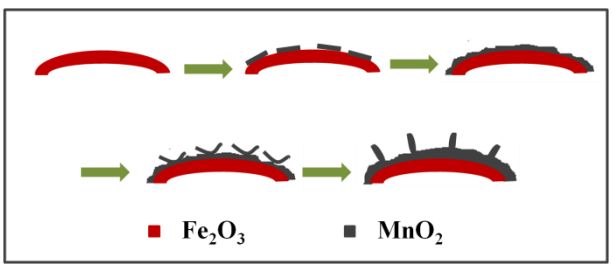

Fig. 6 The possible growth mechanism diagram of the MnO_2@Fe_2O_3 nanospindle.

The electrochemical performance of the MnO_2@Fe_2O_3 nanocomposites with different MnO_2 content is shown in Fig. 7. The CVs of the nanocomposites with different contents of MnO_2 at the

scan rate of 1 mV s^{-1} (Fig. 7a) show that there are two pairs of redox peaks except for that with 60 wt.% MnO_2, indicating that the redundant MnO_2 coating will conceal the Faradaic behavior of Fe_2O_3.

This can also be evidenced from the cycling performance (Fig. 7b). After decorated by MnO_2 nanoflakes, the nanocomposite presents improvements in the specific capacitance and the cycling performance. It is apparent that 40 wt.% MnO_2@Fe_2O_3 presents the best performance with the specific capacitance of 159 F g^{-1} at the current density of 0.1 A g^{-1} because of its uniform structure, much higher than the maximum capacitance of the pristine Fe_2O_3 (55.1 F g^{-1}). The specific capacitance is calculated according to the following equation:[39]

$$C = I \Delta t / (m\Delta V) \qquad (3)$$

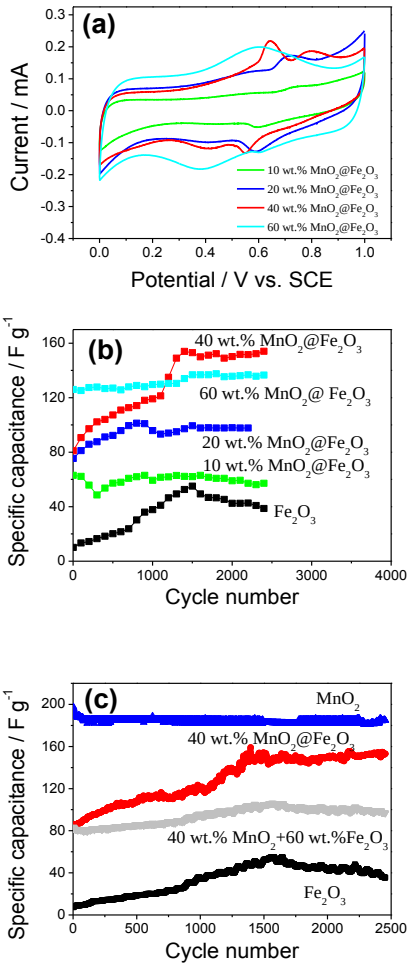

Fig. 7 Electrochemical performance of the prepared MnO_2@Fe_2O_3 nanocomposites with different MnO_2 content: (a) CV curves at the scan rate of 1 mV s^{-1}, (b) cycling performance at the current density of 0.1 A g^{-1}, and (c) the cycling performance of the pristine Fe_2O_3, the MnO_2@Fe_2O_3 nanocomposite and pristine MnO_2.

where I (mA) is discharge current, Δt(s) is discharge time, m(mg) is the mass of the active material, and ΔV(V) is the potential window. From Fig. 7c, it can be clearly observed that the capacitance for both the pristine Fe_2O_3 and the MnO_2@Fe_2O_3 nanospindle increases gradually at the beginning, it was reported that there is an initial activation process for Faradaic pseudocapacitance of Fe_2O_3.[40,41] It is noteworthy that after stabilizing, the specific capacitance of pristine Fe_2O_3 electrode decays 36.0% while that of composite electrode is only 3.84% loss after 1000 cycles, illustrating the excellent long-term cyclability of the composite electrode. The pristine MnO_2 material prepared by the same hydrothermal reaction with $KMnO_4$ can deliver the maximum specific capacitance of 197 F g^{-1}. In addition, we simply mixed pristine Fe_2O_3 and MnO_2 together as active materials with the same ratio of MnO_2 40 wt.%. The electrochemical performance of the mixture was also measured under the same condition. It delivers a specific capacity of 125 F g^{-1}, which is much smaller than that of the 40 wt.% MnO_2@Fe_2O_3 nanospindle (159 F g^{-1}), further confirming there is a synergistic action between MnO_2 and Fe_2O_3. The core-shell MnO_2@Fe_2O_3 nanospindles we designed can provide a lot of interspaces between MnO_2 and Fe_2O_3 to facilitate the diffusion of electrolyte. It is widely accepted that this is the main reason for the superior capacitive performance.[42,43]

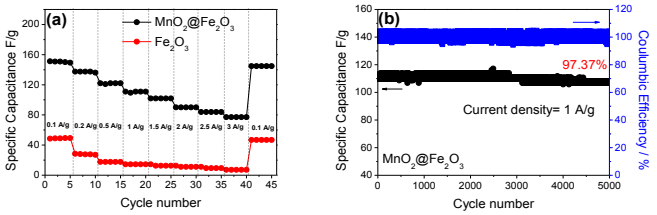

Fig. 8 (a) Comparison between the normalized capacities of the rate performance of the prepared pristine Fe_2O_3 spindles and the 40 wt.% MnO_2@Fe_2O_3 nanospindles, (b) cycling performance of the 40 wt.% MnO_2@Fe_2O_3 nanospindles at the current density of 1 A g^{-1}.

The rate performance of the pristine Fe_2O_3 and the MnO_2@Fe_2O_3 nanospindle from 0.1 A g^{-1} to 3 A g^{-1} is shown in Fig. 8a. Remarkably, even the current density reaches up to 3 A g^{-1}, the specific capacitance of the nanospindle is still maintained at 80 F g^{-1}, much better than the pristine Fe_2O_3. Especially, it is can be seen in Fig. 8b, the MnO_2@Fe_2O_3 nanospindle shows excellent cycling performance with a specific capacitance of 110 F g^{-1} at a high current density of 1 A g^{-1}. The overall specific capacitance retention is 97.4% after 5000 cycles. This means that the open nanoarchitecture ensures efficient contact between electroactive materials and electrolyte even at high rates. The SEM micrographs of the pristine Fe_2O_3 spindles and the 40 wt.% MnO_2@Fe_2O_3 nanospindles after 5000 cycles are shown in Fig. 9a and b, it is shown that the pristine Fe_2O_3 spindles has been partly damaged, causing small nanoparticles. However, the morphology of the 40 wt.% MnO_2@Fe_2O_3 nanospindles is almost intact, that is to say, the configuration is more stable by the twining shell of MnO_2 nanoflakes, which could prevent the possible dissolution of Fe effectively to ensure the content of Fe_2O_3, [4,6] in favour of an improved cycling stability. This is superior to amorphous Fe_2O_3 nanotubes or porous Fe_2O_3 coated with MnO_2, whose capacitance fades with cycling.[32,44] In addition, MnO_2 nanoflakes twined around Fe_2O_3 spindles can make ions penetrate through MnO_2 to intercalate into the Fe_2O_3 core conveniently, which is crucial for the Faradaic reactions of transition

metal oxides. The synergistic effect of the MnO_2@Fe_2O_3 nanospindles is schematically shown in Fig. 9c.

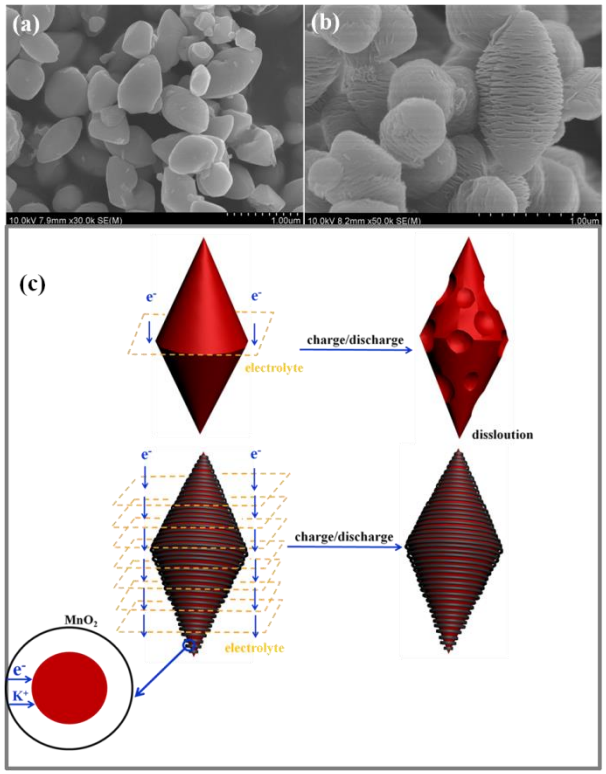

Fig. 9 The SEM micrographs of (a) the pristine Fe_2O_3 spindles and (b) the 40 wt.% MnO_2@Fe_2O_3 nanospindles after 5000 cycles, (c) the synergistic effect of the MnO_2@Fe_2O_3 nanospindles.

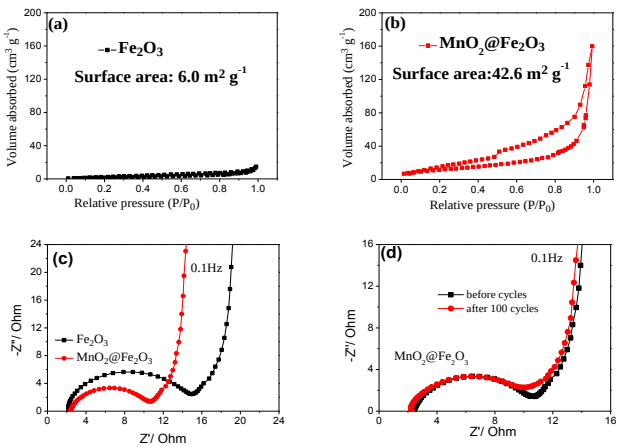

Fig. 10 Nitrogen absorption/desorption results of (a) the prepared pristine Fe_2O_3 spindles and (b) the 40 wt.% MnO_2@Fe_2O_3 nanospindles, (c) AC impedance spectra of the prepared pristine Fe_2O_3 spindles and the 40 wt.% MnO_2@Fe_2O_3 nanospindles , and (d) AC impedance spectra of the MnO_2@Fe_2O_3 electrode before and after 100 cycles.

The BET measurements for the surface areas before and after the decoration of MnO_2 nanoflakes (Fig. 10a and 10b) show that the surface area of the 40 wt.% MnO_2@Fe_2O_3 nanocpupas is 42.6 m^2 g^{-1}, much higher than that of the pristine Fe_2O_3 spindles (6.0 m^2 g^{-1}), providing more active sites for the reversible reactions.

From the EIS curves (Fig. 10c and 10d), it can be noticed that after the decoration of MnO_2 nanoflakes the ion diffusion resistance is decreased, which can make ions penetrate through MnO_2 to intercalate into the Fe_2O_3 core more conveniently. Besides, the diameter of the semicircle decreases slightly after 100 cycles, indicating that initial cycling can activate the electrode effectively, further transfer electrolyte to the inner region of the electrode, which greatly favors the redox processes.

To further study the power density and energy density of the supercapacitors. We assembled a two-electrode full cell with the active carbon (AC) as the negative electrode and the MnO_2@Fe_2O_3 as the positive electrode. Fig. 11 shows the Ragone plot (power density vs. energy density) of the supercapacitors. It is worthy to note that the maximum energy density obtained is as high as 43.8 Wh kg^{-1} at a power density of 110 W kg^{-1} and maintain an energy density of 21.4 Wh kg^{-1} even at a high power density of 3500 W kg^{-1}, which is superior to Pd-acid batteries, Ni-MH batteries and other traditional energy storing devices including aqueous asymmetric supercapacitors.[4,45,46]

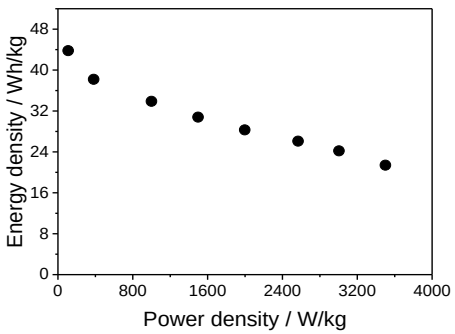

Fig. 11 Ragone plot of the supercapacitors assembled with the 40 wt.% MnO_2@Fe_2O_3 nanospindle and activated carbon as the positive and negative electrodes.

Conclusions

In summary, a unique core-shell MnO_2@Fe_2O_3 nanospindle has been synthesized successfully just by a simple and cost-effective hydrothermal method, which plays a big role for increasing the surface area and active sites for Faradaic reactions. The electrochemical performance of the cheap Fe_2O_3 as the positive electrode for supercapacitors in friendly neutral K_2SO_4 aqueous electrolyte is greatly improved. Its specific capacitance is up to 159 F g^{-1} at a current density of 0.1 A g^{-1} and its maximum energy density in combination with the activated carbon as the negative electrode is up to 43.8 Wh kg^{-1}. The capacitance retention is 97.4% after 5000 cycles at a current density of 1 A g^{-1}. The outstanding capacitive performance is attributed to the fabricated unique structure, which can not only deliver large surface area for redox reactions but also facilitate the diffusion of electrolyte to accelerate the reaction kinetics of Fe_2O_3. In addition, the stable MnO_2 nanoflake shell prevents the capacitance fading of Fe_2O_3. Furthermore, the special core-shell structure with MnO_2 nanoflakes

twined provides a synergetic effect to increase the capacitance, and 40 wt.% MnO_2@Fe_2O_3 is the optimal composition. The results above suggest that such a core-shell MnO_2@Fe_2O_3 nanospindle is appealing for supercapacitors in the future by its virtue of high-performance, low-cost and environmental friendliness.

Acknowledgement: Financial support from China National Funds for Distinguished Young Scientists (NSFC No. 51425301) and STCSM (14520721800) is greatly appreciated.

References and notes:

Same contributions to this work.

1 A. S. Aric`o, P. Bruce, B. Scrosati, J. M. Tarascon and W. van Schalkwijk, *Nat. Mater.*, 2005, **4**, 366-377.

2 G. F. Ma, M. M. Dong, K. J. Sun, E. Feng, H. Peng and Z. Q. Lei, *J. Mater. Chem. A*, 2015, **3**, 4035-4041.

3 R. Väli, A. Laheäär, A. Jänes and E. Lust, *Electrochim. Acta.* 2014.**121**, 294-300.

4 F. X. Wang, S.Y. Xiao, Y.Y. Hou, C. L. Hu, L. L. Liu and Y. P. Wu, *RSC Advances*, 2013, **3**, 13059-13084.

5 T. Wei, R. Zeng, Y. M. Sun, Y. H. Huang and K. V. Huang, *Chem. Commu.*, 2014, **590**, 162-1964.

6 Q. T. Qu, P. Zhang, B. Wang, Y. H. Chen, S. Tian, Y. P. Wu and R. Holze, *J. Phys. Chem. C*, 2009, **113**, 14020-14027.

7 Q. T. Qu, B. Wang, L. C. Yang, Y. Shi, S. Tian and Y. P. Wu, *Electrochem. Commun.* 2008, **10**, 1652-1655.

8 M. P. Bichat, E. Raymundo-Piñero and F. Béguin, *Carbon*, 2010, **48**, 4351-4361.

9 K. Fic, M. Meller and E. Frackowiak, *Electrochim. Acta*, 2014, **128**, 210-217.

10 J. Shao, X. Li, Q. T. Qu and Y. P. Wu, J. Power Sources, 2013, 223, 56-61.

11 D. J. Lee, J. Choi, M. H. Ryou, C. H. Kim, Y. M. Lee and J. K. Park, *J. Mater. Chem. A*, 2014, **2**, 2906-2909.

12 W. T. Gu, M. Sevilla, A. Magasinski, A. B. Fuertes and G. Yushin, *Energ. Environ.Sci.*, 2013, **6**, 2465-2476.

13 Y. Zhu, S. Murali and M. D. Stoller, *Science*, 2011, **332**, 1537-1541.

14 D. Pech, M. Brunet, H. Durou, P. H. Huang, V. Mochalin, Y. Gogotsi, P. L. Taberna and P. Simon, *Nat. Nanotechnol.*, 2010, **5**, 651-654.

15 D. Hulicova-Jurcakova, A. M. Puziy, O. I. Poddubnaya, F. SuarezGarcia, J. M. D. Tascon and G. Q. Lu, *J. Am. Chem. Soc.*, 2009, **131**, 5026-5027.

16 J. Xu, Q. F. Wang, X. W. Wang, Q. Y. Xiang, B. Liang , D. Chen and G. Z. Shen, *ACS nano*, 2013, **7**, 5453-5462.

17 I. Ryu, M. H. Yang, H. Kwon, H. K. Park, Y. R. Do, S. B. Lee and S. Y. Yim, *Langmuir*, 2014, **30**, 1704-1709.

18 X. Lu, G. Wang, T. Zhai, M. Yu, J. Gan, Y. Tong and Y. Li, *Nano Lett.*, 2012, **12**, 1690-1696.

19 R. Li, X. Ren, F. Zhang, C. Du and J. P. Liu, *Chem. Commun.*, 2012, **48**, 5010-5012.

20 Y. J. Wu, G. H. Gao and G. M. Wu, *J. Mater. Chem. A*, 2015, **3**, 1828-1832.

21 L. Hou, C. Yuan, L. Yang, L. Shen, F. Zhang and X. Zhang, *RSC Adv.*, 2011, **1**, 1521-1526.

22 Z. P. Liu, R. Z. Ma, M. Osada, K. Takada and T. Sasaki, *J. Am. Chem. Soc.*, 2005, **127**, 13869-13874.

23 L. Zhu, W. Y. Wu, Y. S. Zhu, W. P. Tang and Y. P. Wu, *J. Phys. Chem. C*, 2015, **119**, 7069-7075.

24 X. W. Wang, M. X. Li, Z. Chang, Y. Q. Yang, Y. P. Wu and X. Liu, *ACS Appl Mater Interfaces.*, 2015, 7, 2280-2285.

25 T. Brezesinski, J. Wang, S. H. Tolbert and B. Dunn, *Nat. Mater.*, 2010, **9**, 146-151.

26 C. Yuan, X. Zhang, L. Su, B. Gao and L. Shen, *J. Mater. Chem. A*, 2009, **19**, 5772-5777.

27 W. W. Zhou, D. Z. Kong, X. T. Jia, C.Y. Ding, C.W. Cheng and G. W. Wen, *J. Mater. Chem. A*, 2014, **2**, 6310-6315.

28 S. J. Zhu, J. Q. Jia, T. Wang, D. Zhao, J. Yang, F. Dong, Z. G. Shang and Y. X. Zhang, *Chem. Commun.*, 2015, doi: 10.1039/C5CC03976B.

29 Y. F. Zhang, L. Q. Li, H. Q. Su, W. Huang and X. C. Dong, *J. Mater. Chem. A*, 2015, **3**, 43-59.

30 C. R. Xiong, A. E. Aliev, B. Gnade, K. J. Balkus, *ACS nano*, 2008, **2**, 293-301.

31 W. Li, K. Xu, B. Li, J. Sun, F. Jiang, Z. Yu, R. Zou, Z. Chen and J. Hu, *ChemElectroChem.*, 2014, **1**, 1003-1008.

32 D. Wang, Q. Wang and T. Wang, *Nanotechnology.*, 2011, **22**, 135604.

33 N. Nagarajan and I. Zhitomirsky, *J. Appl. Electrochem.*, 2006, **36**, 1399-1405.

34 D. Sarkar, G. G. Khan, A. K. Singh and K. Mandal, *J. Phys. Chem. C*, 2013, **117**, 15523-15531.

35 H. Li, Q. D. Zhao, X.Y. Li, Y. Shi, Z. R. Zhu, M. Tade and S.M. Liu, *Mater. Res. Bull.*, 2012, **47**, 1459-1466.

36 S. Chaudharia and M. Srinivasan, *J. Mater. Chem.*, 2012, **22**, 23049-23056.

37 R. Ma, Y. Bando, L. Zang and T. Sasaki, *Adv. Mater.*, 2004, **16**, 918-922

38 L. Bao, J. Zang and X. Li, *Nano Lett.*, 2011, **11**, 1215-1220.

39 T. Yan, Z. J. Li, R. Y. Li, Q. Ning, H. Kong, Y. L. Niu and J. K. Liu, *J. Mater. Chem. A*, 2012, **22**, 23587-23592.

40 R. B. Rakhi, W. Chen, D. Cha and H. N. Alshareef, *Nano Lett.*, 2012, **12**, 2559-2567.

41 C. Z. Yuan, J. Y. Li, L. R. Hou, X. G. Zhang, L. F. Shen and X. W. Lou, *Adv. Funct. Mater.*, 2012, **22**, 4592-4597.

42 X. Zhang, W. Shi and J. Zhu, *Nano Res.*, 2010, **3**, 643-652.

43 T. Y. Kim, G. Jung, S. Yoo, K. S. Suh and R. S. Ruoff, *ACS Nano*, 2013, **7**, 6899-6905.

44 P. H. Yang, Y. Ding, Z. Y. Lin, Z. W. Chen, Y. Z. Li, P. F. Qiang, M. Ebrahimi, W. J. Mai, C. P. Wong and Z. L. Wang, *Nano Lett.*, 2014, **14**, 731-736.

45 Y. Liu, H. Pan, M. Gao and Q. Wang, *J. Mater. Chem. A*, 2011, **21**, 4743-4755.

46 J. M. Tarascon and M. Armand, *Nature*, 2001, **414**, 359-367.

Table of content

Core-shell MnO_2@Fe_2O_3 nanospindles as positive electrode for aqueous supercapacitors

Lei Zhu, Zheng Chang, Yanfang Wang, Bingwei Chen, Yusong Zhu, Weiping Tang and Yuping Wu

A novel core-shell type MnO_2@Fe_2O_3 nanospindle has been synthesized by twinning MnO_2 nanoflakes around spindle-like Fe_2O_3 particles uniformly, exhibiting superior capacitance and excellent electrochemical performance stability.